

Measurement of the infrared magneto-optic properties of thin-film metals and high temperature superconductors

J. Černe^{a)}

Department of Physics, University at Buffalo, The State University of New York, Buffalo, New York 14260 and Department of Physics, University of Maryland, College Park, Maryland 20742

D. C. Schmadel

Department of Physics, University of Maryland, College Park, Maryland 20742

L. B. Rigal

Laboratoire National des Champs Magnétiques Pulsés, Toulouse, France and Department of Physics, University of Maryland, College Park, Maryland 20742

H. D. Drew

Department of Physics, University of Maryland, College Park, Maryland 20742 and Center of Superconductivity Research, University of Maryland, College Park, Maryland 20742

(Received 22 May 2003; accepted 16 July 2003)

A sensitive polarization modulation technique uses photoelastic modulation and heterodyne detection to simultaneously measure the Faraday rotation and induced ellipticity in light transmitted by semiconducting and metallic samples. The frequencies measured are in the midinfrared and correspond to the spectral lines of a CO₂ laser. The measured temperature range is continuous and extends from 35 to 330 K. Measured samples include GaAs and Si substrates, gold and copper films, and YBCO and BSCCO high temperature superconductors. © 2003 American Institute of Physics. [DOI: 10.1063/1.1619582]

I. INTRODUCTION

Conventional dc Hall effect measurements in novel electronic materials such as high temperature superconducting cuprates (HTSC) have been essential in revealing the unusual character of these systems.¹ Extending these measurements to higher frequencies^{2,3} allows one to probe more effectively the energy scales of the system (e.g., plasma frequency, cyclotron frequency and carrier relaxation rates), and provides greater insight into the intrinsic electronic structure of systems ranging from conventional Fermi liquid metals⁴ to more exotic metals such as HTSC (Ref. 5) and other transition metal oxides.⁶

Magnetopolarimetry measurements can be used to extend Hall effect measurements into the infrared frequency range (10¹³ Hz). These measurements are sensitive to the complex Faraday angle θ_F , which is closely related to the complex Hall angle θ_H .⁷ Though θ_F and θ_H tend to be small for metals in the midinfrared (MIR, 900–1100 cm⁻¹), there are a number of advantages in performing these higher frequency measurements. First, the high frequency allows one to avoid impurity scattering or grain boundary effects, which may dominate lower frequency Hall measurements. This is especially important in new materials, which often contain many impurities and defects. Furthermore, the MIR measurements allow one to examine the trends observed at lower frequencies. Since $\tan \theta_H$ (and θ_H) obeys a sum rule,³ it is very useful to be able to integrate θ_H to higher frequencies to verify whether (and where) the Hall angle sum rule saturates

or whether there is more relevant physics at even higher frequencies. Finally, since the high frequency behavior of θ_H is constrained by the general requirements of response functions, a simple, model-independent asymptotic form for θ_H becomes more accurate at higher frequencies.

In this article, we present a sensitive midinfrared polarimetry technique, which uses photoelastic modulation and heterodyne detection, and which can be used to explore a variety of materials.^{8,9} In what follows, we shall first introduce the hardware components and describe their operation, next we shall present an analysis of both the operation and data, and finally, we shall present recent results on semiconductors, metal films, and HTSC.

II. EXPERIMENTAL SYSTEM

A. Overview

The experimental system of the current work measures the real and imaginary parts of θ_F using a linearly polarized CO₂ laser beam. Figure 1 schematically illustrates the optical path in which linearly polarized light from the CO₂ laser, after encountering various steering and attenuation components, proceeds through lens 1, which focuses it to a point at the chopper. The chopper impresses onto the intensity of the beam a temporal square wave modulation of $f_0 \approx 112$ Hz, which will later facilitate the removal of laser power variations using ratios. Lens 2 then refocuses the emerging beam so as to eventually produce a focused diffraction spot on the surface of the sample. The intervening element, a film polarizer, purifies the beam's polarization, removing any contamination caused by the chopper, attenuators, etc. It is this

^{a)}Electronic mail: jcerne@nsm.buffalo.edu

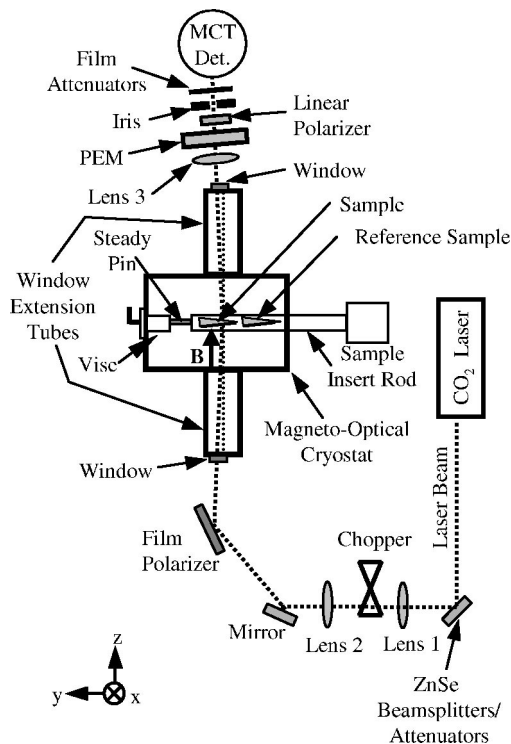


FIG. 1. Overall schematic of the optical path. The dotted line represents the CO₂ laser beam. The CO₂ laser and the first four optic elements are actually located on a separate mount detached from the optical table.

highly linearly polarized beam, which after passing through the ZnSe magnet housing window encounters the sample as shown in Fig. 2. The sample will reflect, absorb, and transmit portions of this beam. The polarization of the transmitted beam will have sustained a Faraday rotation and ellipticity proportional to the magnetic field B and consistent with the physics peculiar to the sample. We shall assign the x axis to the initial polarization direction and the z axis to the direction of propagation.

The Faraday angle includes both real and imaginary terms. The real term corresponds to a simple geometric rotation of the polarization vector about the direction of propagation. The imaginary term relates directly to the ellipticity of the polarization. Since the sample is axially symmetric along B , the transmittance tensor is diagonal when represented in the circular polarization basis. Therefore, changes

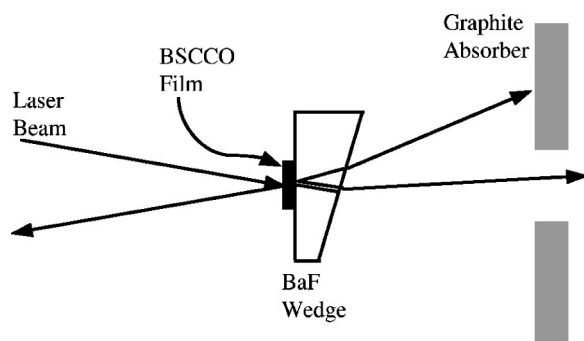


FIG. 2. Wedged sample and beam path. The paths of the reflected beams are sufficiently separated by the 2° wedge to prevent their entering the detection system or reentering the laser.

in the incident polarization only depend on: (1) the relative difference in the phase of left versus right circularly polarized light due to $\text{Re}(\theta_F)$, which leads to a rotation [circular birefringence or Faraday rotation (FR)] in the linearly polarized incident light; and (2) the relative difference in the transmission of left versus right circularly polarized light due to $\text{Im}(\theta_F)$, which introduces ellipticity [circular dichroism (CD)] to the linearly polarized incident light.

The magnitude of θ_F at CO₂ wavelengths is about 10^{-4} rad. As such, one may consider the electric vector along the y axis to be a feeble signal added to the strong signal of the original electric field vector along the x axis. This small signal cannot be measured directly by the common method of crossed polarizers because the power in the field polarized along the y axis is proportional to the square of θ_F or 10^{-8} times the power in the original beam in the x polarization. Clearly, leakage of the input beam through either polarizer would effectively direct power into the y axis polarization, which would overwhelm any amount introduced by the sample. The natural choice in such instances is heterodyne detection.

Heterodyne detection produces cross terms, which are proportional to the electric vector along the y axis rather than its square. We realize heterodyne detection by phase modulating the electric vector along the y axis using a photoelastic modulator (PEM). The PEM is a model PEM-90 series II ZS50 manufactured by Hinds Instruments, Inc., with a modulation frequency of $f_m = 50$ kHz (angular frequency $\omega_m = 2\pi f_m$). It comprises essentially a block of ZnSe and a piezoelectric transducer, which creates the stress alternations at a frequency of 50 kHz and ultimately the phase modulation of the light beam. The electric vector along the x axis is essentially unaffected by the PEM.

The beam emerges from the PEM and then strikes a polarizer on a 45° angle, which allows a portion of the electric vector from each of the y and x directions to contribute to that which emerges now at a 45° angle. These two contributions after being mixed by the detector produce the 50 kHz PEM frequency along with sidebands. The amplitude of each of the sidebands is proportional to the electric vector along the y axis and also proportional to the corresponding Bessel function, whose argument is the depth of the PEM modulation. In fact, as will be derived below, the even sidebands or harmonics are proportional to $\text{Re}(\theta_F)$ and the odd sidebands or harmonics are proportional to $\text{Im}(\theta_F)$.

In the following sections we consider certain elements or subassemblies of the experimental system in detail beginning with the CO₂ laser.

B. CO₂ laser

The CO₂ laser, a model PL5 manufactured by Edinburgh Instruments, Ltd., provides a number of spectral lines ranging from 9.174 to 10.860 μm (1090 to 920 cm^{-1}), any one of which is selected by a grating internal to the cavity. A separate CO₂ laser spectrometer verifies the wavelength of each line. The direction of the beam exiting the laser, however, differs for different lines sometimes by nearly as much as one half of a spatial mode. Without realignment the result

would be a spatial shift of the diffraction spot at the sample by as much as one half of a spot diameter. The small size of a sample can aggravate the sensitivity of the system to such slight misalignment particularly when such changes cause the beam to wander off or even near the edge of the sample. Lens 3 essentially focuses an image of the sample onto the iris shown in Fig. 1 and may be used as an aid in regaining alignment as is necessary to compile valid relative frequency data. The design and construction of the hardware ensure that the relative position of the sample, lens 3, and the iris are constant. Therefore, adjusting the laser beam steering to maximize the power through the iris after each laser line change likewise ensures that the beam is passing through the same area of the sample. While taking data, the iris is dilated to accommodate a small amount of beam wander.

Another consideration of the laser is the high output power (2–30 W). Three attenuators reduce the power ~ 30 dB to avoid heating the sample while still producing a strong signal within the linear range of the mercury cadmium telluride (MCT) detector. These attenuators are ZnSe windows having an antireflection coating on one side. They replace mirrors in the beam steering assemblies with the uncoated side serving as the reflective surface. Each of these attenuators introduces approximately 10 dB of loss.

To reduce noise due to temporal fluctuations in the laser output power, the Faraday signals at harmonics of ω_m are normalized by the laser power level, which is sampled at ω_0 . The current experiment employs the usual method of source compensation,¹⁰ which involves the chopper along with an additional lock-in amplifier. Note, also, that the heterodyne detection system described above permits use of the same detector for the power level sample as well as the second and third harmonics of ω_m . This feature eliminates the wavelength dependence of the detector, and thus facilitates accurate relative measurements of the wavelength dependence of the complex θ_F . A final consideration regarding the laser involves its placement with respect to the magnet. The particular position of the laser is perpendicular to the magnetic field and at such a distance as to reduce detuning of the laser cavity caused by magnetostriction to a tolerable amount.

C. Magnet system and sample mounting

The optical magnet system (an 8 T, split coil, Helmholtz Spectromag, manufactured by Oxford Instruments PLC) involved a side-loading sample cold finger, with the sample located in vacuum. Therefore, no cold windows are required, which proved to be advantageous for these measurements. The main modifications to the magnet system involved the external windows, the sample handling hardware, and the internal bore tube shielding. To understand the modifications to the external windows, consider that the wavelength range of interest requires ZnSe windows. However, the band gap of ZnSe is only 2.7 eV, and the magnetic field of 2 T at the original location of the windows caused a significant Faraday rotation, which overwhelmed that of the sample. The 35-cm-long aluminum extension tubes locate the windows where the magnetic field is less than 0.1 T. The remaining Faraday rotation background is thus reduced to the same order as that

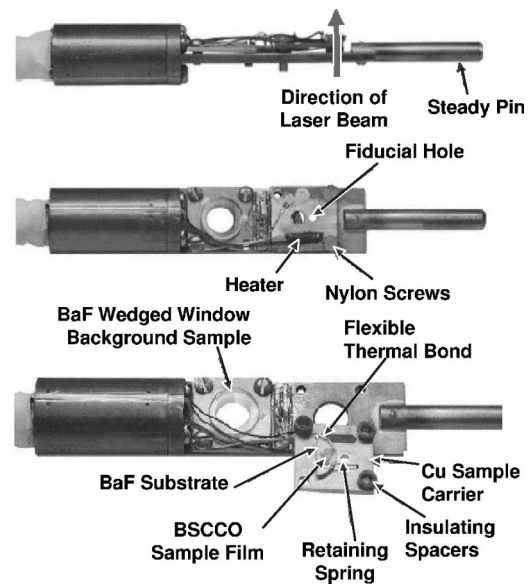


FIG. 3. Sample mount assembly.

of the sample, and having been carefully measured for different wavelengths, can be easily removed from the data at a later time. For magnets requiring cold windows located within the high field region the background may be reduced by using a material with a higher band gap such as BaF. The sample handling hardware was extensively modified. The effort included adding a steady pin and vise, implementing a more responsive temperature control system, and developing a near stress-free sample mount. The steady pin, depicted in Fig. 3 protrudes from the blade of the original sample stick to which it is brazed. The vise, located within the magnet housing, engages the pin using a Teflon collet. This combined apparatus restrains the sample stick against the forces induced by the magnetic field, and thus prevents the large, extraneous interference signals resulting from changing multipaths and étalons.

Figure 3 also depicts parts of the new temperature control system, which comprises a heater and a cooling link. The heater is a $400\ \Omega$ $\frac{1}{4}$ W metal film resistor potted into the copper sample carrier using 2850FT epoxy with catalyst 9, both of which are manufactured by Emerson & Cuming. The cooling link is simply a 4 cm length of 22 gauge copper wire connecting the copper sample carrier to the blade of the original sample stick from which it is otherwise thermally insulated by spacers and nylon screws. The operation is simple: Liquid helium delivered to the sample stick by the original provision, cools the blade to about 10 K, and the cooling link cools the copper sample carrier. Current delivered to the resistor in an easily controlled fashion can provide up to 2 W of heat to the copper sample carrier. Because of the low thermal mass of both the copper sample carrier and the link, a compromise temperature emerges within about 1 min. Sweeping the temperature entails nothing more than adjusting the current. An important advantage of this system is that only the rather small copper sample carrier changes temperature. The remaining hardware, remaining essentially constant in temperature, has a greatly reduced ten-

dency to adversely affect the measurement by moving or warping.

The near stress-free sample mount consists of a phosphor bronze wire retaining spring and a thermally conductive flexible silver-filled RTV known as Eccobond 59C manufactured by Emerson & Cuming, Inc. The particular sample shown attached to the sample stick is a small irregularly shaped film of optimally doped $\text{Bi}_2\text{Sr}_2\text{Ca}_1\text{Cu}_2\text{O}_{8+\delta}$ approximately 200 nm thick, which had been peeled from a single bulk crystal. This small film was placed against a polished surface of a BaF crystal, which serves as a substrate and maintains the temperature of the sample. Van der Waal force holds the film in place. A 2° wedge of the BaF substrate eliminates étalon effects. Only one of the two corners of the substrate is cemented to the copper sample carrier. The phosphor bronze retaining spring lightly holds the other corner while allowing some motion to relieve the stress caused by dissimilar thermal expansion coefficients. Without this provision the stress induced in the substrate had caused overwhelming and unpredictable complex Faraday rotations. It is this stress-free mounting which actually facilitated the fast temperature scans required to eliminate $1/f$ noise apparent in previous work. The copper sample carrier is provided with a small fiducial hole, also shown in Fig. 3. Prior to insertion of the sample stick into the magnet the sample's position is accurately measured with respect to this hole. After insertion, the fiducial hole is located using the transmitted intensity of the laser beam. The sample is then positioned within the beam by raising or lowering the magnet and sliding the sample stick in or out. Finally, the new reentrant bore tubes are fitted with graphite plates to absorb the stray radiation scattered from the incident laser beam by the various reflective surfaces, e.g., sample, substrate, magnet windows, etc.

D. Optical table components

The remaining items of Fig. 1, which along with the magnet are located on an aluminum optical table, will receive consideration within this section. Among these items are the chopper and lens 1. As explained earlier, the chopper impresses upon the beam a square wave amplitude variation of $f_0=112$ Hz. Lens 1 participates in this task by focusing the beam to a point at the chopper blades, optimizing the sharpness of the modulation. This prevents spatial variations within the beam from causing phase and amplitude errors in the reported laser power level.

Also of particular importance is a pivot platform upon which sits the optical detection system. Two aluminum box beams connect this platform to a vertical pivot located directly below the sample. When the two clamps securing the platform to the optical table are loosened the platform may be rotated about the vertical axis of the pivot. This motion is necessary to align the detection system to both the fiducial hole and wedged substrates, which bend the laser beam about the same axis by an amount depending on the substrate wedge angle and its index of refraction.

E. Optical detection system

The first component encountered by the laser beam after exiting the second magnet window is lens 3, which focuses an image of the sample onto the iris as previously discussed. This lens joins with the PEM and polarization analyzer in an assembly, which can be rotated as a single unit about the input optical axis, which is the z axis. Such a rotation is equivalent to a real, but opposite, Faraday rotation, at least for sufficiently small angles so that the polarization sensitivity of the MCT detector is not apparent. Fixed calibration rotation stops limit this rotation to a known amount, thus serving as a Faraday rotation calibrator. To calibrate the Faraday rotation signal, one rotates the assembly the known amount and uses this to scale the empirical values for each wavelength, as will be discussed in Sec. III D.

Another important consideration involves reflection at the surfaces of the ZnSe interaction block of the PEM. A reflected beam, which makes additional passes through the ZnSe interaction block, will receive additional modulation. Since, the cross term is a function of the depth of modulation, such triply modulated stray beams can cause significant errors. An antireflection (AR) coating and a tilting of the PEM by 25° reduce and displace reflected beams and, thereby, sufficiently reduce their effect.

A variable selection of polyimide films further attenuate the laser beam so that its power is within the linear range of the MCT detector, which is a model J15D14 MCT detector manufactured by EG&G Judson.

F. Electronic instrumentation

Along with the electronics that attend the magnet, PEM, chopper, etc., the system uses three model 7260 digital signal processing (DSP) harmonic lock-in amplifiers manufactured by EG&G. These lock-ins detect the voltage of a selectable harmonics of the input signal. This feature is essential because, as mentioned, the even harmonics of ω_m are proportional to $\text{Re}(\theta_F)$ and the odd harmonics are proportional to $\text{Im}(\theta_F)$. The first lock-in determines the rms voltage V_0 at the chopper frequency ω_0 and is considered to be the dc reference reflecting the average laser power. The second lock-in determines the rms voltage V_2 at $2\omega_m$, while the third determines the rms voltage V_3 at $3\omega_m$. These three signals are recorded in real time by a local computer, which forms two normalized, dimensionless signals S_2 and S_3 , as shown below:

$$S_2 = \frac{V_2}{V_0}, \quad S_3 = \frac{V_3}{V_0}. \quad (1)$$

Since motion of the beam within the PEM aperture changes the phase of the harmonics, only the magnitudes of V_2 and V_3 are used in the signal analysis. Unlike $V_2(t)$ and $V_3(t)$, which are sinusoidal functions, $V_0(t)$ is a square wave and, therefore, its amplitude will be undervalued by the DSP lock-in. Since the DSP lock-in uses a sinusoidal reference, it only senses the fundamental harmonic component of the square wave.¹¹ To correct this error, the V_0 signal is multiplied by $4/\pi$, which is the factor that relates the first harmonic of a square wave to the amplitude of the square wave. There are two reasons for using S_3 instead of S_1 (the

signal at the fundamental frequency ω_m), despite the fact that S_1 is typically larger than S_3 and provides the same information. S_1 is more susceptible to electronic noise from the PEM power supply and transducers, which operate at ω_m . Furthermore, the thickness of the PEM's ZnSe optical head is also modulated at ω_m , causing an étalon interference modulation signal at the fundamental frequency. S_2 and S_3 will be used to determine $\text{Re}(\theta_F)$ and $\text{Im}(\theta_F)$, respectively, as will be shown in Sec. III A.

III. ANALYSIS

In the analysis of both the system and data we employ two formalisms. One concerns the representation and transformation of the polarization state of light and the other concerns the transmission and reflection response of multilayer stacks with complex material properties, σ , ϵ , or μ . Both are presented as appendices.

A. θ_F versus normalized lock-in signals

For light initially propagating in the z direction and polarized along the x axis, we define the Faraday angle as

$$\theta_F = \arctan \frac{t_{yx}}{t_{xx}} \approx \frac{t_{yx}}{t_{xx}}, \quad (2)$$

where t_{xx} is the field transmission along the x polarization, t_{yx} is the field transmission along the y polarization, and the arctan function was dropped because of the very small angles involved in the current work. As such, it represents the complex amplitude (amplitude and phase) in the y polarization having been derived from the incident radiation in the x channel. One will recognize $\text{Re}(\theta_F)$ as the geometric rotation of the incoming polarization and $\text{Im}(\theta_F)$ as the ellipticity.

Consider next that the experimental system examines the light transmitted by the sample, which results from incident light initially polarized along the x axis. A simple matrix equation represents this activity in the linear polarization basis as

$$\begin{pmatrix} t_{xx} & t_{xy} \\ t_{yx} & t_{yy} \end{pmatrix} \begin{pmatrix} x_{\text{in}} \\ 0 \end{pmatrix} = \begin{pmatrix} x_{\text{out}} \\ y_{\text{out}} \end{pmatrix}, \quad (3)$$

where x_{in} , x_{out} , and y_{out} are the complex amplitudes of the x -polarized incident, x -polarized transmitted, and y -polarized transmitted electric fields, respectively. Assuming the a and b axes of the sample to be indistinguishable, i.e., near square symmetry, and noting that the B field is uniform and parallel to the z axis, we know that the sample transmission of Eq. (3) will be diagonal in the circular basis. Using the polarization formalism in the Appendix, the sample can be represented as

$$\begin{pmatrix} t_p & 0 \\ 0 & t_n \end{pmatrix} = \begin{pmatrix} t_{xx} - it_{yx} & 0 \\ 0 & t_{xx} + it_{yx} \end{pmatrix}, \quad (4)$$

where t_p is the transmission coefficient corresponding to positive helicity (positive $\hat{\phi}$ rotation seen at fixed point for a wave traveling in the positive z direction), and t_n is the transmission coefficient corresponding to negative helicity (nega-

tive $\hat{\phi}$ rotation seen at fixed point for a wave also traveling in the positive z direction). Transforming back to the linear basis the sample matrix becomes

$$\begin{pmatrix} t_{xx} & t_{xy} \\ t_{yx} & t_{yy} \end{pmatrix} = \begin{pmatrix} t_{xx} & -t_{yx} \\ t_{yx} & t_{xx} \end{pmatrix},$$

which is considerably simpler. It is also useful to note that by the definition in Eq. (2) the Faraday angle relates very simply to the ratio of the transmissions of the right and left circular polarization:

$$\begin{pmatrix} \frac{t_p}{t_n} & 0 \\ 0 & \frac{t_n}{t_p} \end{pmatrix} = \begin{pmatrix} e^{-i 2 \theta_F} & 0 \\ 0 & e^{i 2 \theta_F} \end{pmatrix}.$$

Next, for the purpose of developing a relation between the sample transmission and the lock-in outputs consider the relevant experimental elements represented schematically as

$$\begin{aligned} &\text{laser} \rightarrow \text{sample} \rightarrow \text{PEM} \rightarrow \text{polarizer at } 45^\circ \\ &\quad \rightarrow \text{square law detector} \rightarrow \text{lock-ins.} \end{aligned}$$

Again, using the polarization formalism, the components in the the first line, which operate on the laser beam $|x\rangle$ may be represented as

$$\mathbf{R}\left(\frac{\pi}{4}\right) \times \begin{pmatrix} 1 & 0 \\ 0 & 0 \end{pmatrix} \times \mathbf{R}^{-1}\left(\frac{\pi}{4}\right) \times \text{PEM} \times \text{sample} \times |x\rangle$$

or

$$\begin{aligned} \begin{pmatrix} \langle p | \text{out} \rangle \\ \langle n | \text{out} \rangle \end{pmatrix} &= \begin{pmatrix} e^{-i(\pi/4)} & 0 \\ 0 & e^{i(\pi/4)} \end{pmatrix} \begin{pmatrix} 1 & 0 \\ 0 & 0 \end{pmatrix} \\ &\times \begin{pmatrix} e^{i(\pi/4)} & 0 \\ 0 & e^{-i(\pi/4)} \end{pmatrix} \begin{pmatrix} 1 & -i \\ 1 & i \end{pmatrix} \\ &\times \begin{pmatrix} e^{i\beta \cos \omega_m t} & 0 \\ 0 & 1 \end{pmatrix} \begin{pmatrix} 1 & 1 \\ i & -i \end{pmatrix} \\ &\times \begin{pmatrix} e^{-i\theta_F} & 0 \\ 0 & e^{i\theta_F} \end{pmatrix} \begin{pmatrix} 1 & -i \\ 1 & i \end{pmatrix} \begin{pmatrix} 1 \\ 0 \end{pmatrix}, \end{aligned}$$

where β is the PEM modulation amplitude. The above signal is incident upon a square-law detector whose output is a voltage proportional to the square of the modulus of the amplitude of the fields:

$$\text{voltage} \propto \langle \text{out} | \text{out} \rangle \propto \text{optical power.}$$

For the small angles considered the multiplication of these matrices along with the Bessel function expansion of $e^{i\beta \cos(2\pi f)}$ produces

$$\text{Re}(\theta_F) = \text{Re}\left(\frac{t_{yx}}{t_{xx}}\right) = -\frac{1}{4J_2(\beta)} S_2, \quad (5)$$

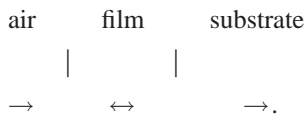
$$\text{Im}(\theta_F) = \text{Im}\left(\frac{t_{yx}}{t_{xx}}\right) = -\frac{1}{4J_3(\beta)} S_3, \quad (6)$$

where $J_2(\beta)$ and $J_3(\beta)$ refer to second and third order Bessel functions, respectively.

B. Sample properties versus θ_F

Since the sample transmission matrix, Eq. (4), is diagonal in the circular polarization basis, each circular polarization channel acts independently and may be treated as such. Indeed, by the same symmetry considerations, the sample matrix representation of the conductivity tensor is also diagonal in the circular basis. In what follows we will develop an expression for the transmission of a sample–substrate combination and then separately apply this expression to each polarization channel. This will determine an expression for the indices of refraction of the film for positive and negative helicity $n_{f,p}$ and $n_{f,n}$, respectively, which are then easily related to σ_{xx} and σ_{xy} .

Figure 2, appearing earlier, depicts the transmission through the sample, which is usually a film–substrate combination. The input beam strikes the sample film, a portion reflects as shown, and a portion propagates into the sample film, and after enduring some absorption arrives in the forward direction at the output side of the film. This portion strikes the interface between the film and the substrate mounting surface. Some reflects back and forth within the sample film and some proceeds as a beam into the wedged substrate, soon reaching the substrate–air interface. Most of this beam propagates into the air eventually arriving at the detection system. Because of the wedge angle of the substrate–air interface, the small reflected portion leaves the optical path and is absorbed by strategically placed graphite slabs located in the magnet’s reentrant bore tubes. For this reason the substrate–air interface does not participate in the Faraday rotation for any of the materials of current interest and need not be considered. All of the relevant activity above can, therefore, be represented schematically as



The formalism for multilayer transmission presented in the appendix represents this sequence generally as

$$(\text{sample}) \begin{pmatrix} E_{\text{air}, \rightarrow} \\ E_{\text{air}, \leftarrow} \end{pmatrix} = \begin{pmatrix} E_{\text{sub}, \rightarrow} \\ 0 \end{pmatrix}, \tag{7}$$

where $(\text{sample}) = \mathbf{S}_{\text{film,sub}} = \mathbf{U}_{\text{film}} \mathbf{S}_{\text{air,film}}$ with \mathbf{S} denoting the interface matrix and \mathbf{U} denoting the propagation matrix. That is, the sample acts on the electric field vectors $E_{\text{air}, \rightarrow}$ and $E_{\text{air}, \leftarrow}$ of the incoming and reflected waves, respectively, on the input side producing the electric field vectors $E_{\text{sub}, \rightarrow}$ and $E_{\text{sub}, \leftarrow}$ of the outgoing and reflected waves on the output side, where, of course, we have no incoming wave. We require only the transmission, which from Eq. (7) is the (1, 1) element of the inverse of the sample matrix. Since the transmission is the same for either propagation direction; one can propagate the light backwards to avoid taking the inverse of the sample matrix. The end result is the transmission is given by the inverse of the (2, 2) element of the sample matrix, which using the relations in the Appendix can be related (after some algebraic manipulation) to the material properties:

$$t(n) = 4n_s n_f e^{ikd} [n_s (e^{i2kd}(n_f - 1) + n_f + 1) - n_f (e^{i2kd}(n_f - 1) - n_f - 1)]^{-1}, \tag{8}$$

where d is the thickness of the film, $k = 2\pi n_f / \lambda$ is the wave number within the film, and n_f and n_s are the indices of refraction of the film and substrate. There is one such equation for each circular polarization channel n and p .

Analysis of the data ultimately requires an equation for the index of refraction (or some other material property) in terms of the Faraday angle. Equation (4) with Eq. (8) contain the pertinent information but the combination does not lend itself to inversion. Fortunately, because the relative difference between the indices of refraction of the film for n and p polarizations is usually very small, we can generate a readily invertible form by expanding their combination about either $n_{f,n}$ or $n_{f,p}$. Choosing $n_{f,p} = n_f$ with $\delta = n_{f,n} - n_{f,p}$, expanding Eq. (4), and keeping only the linear term results in

$$\theta_F = \frac{-i\delta}{2} \frac{1}{t(n_f)} \frac{dt(n)}{dn}. \tag{9}$$

Combining Eqs. (8) and (9) produces

$$\delta = 2\theta_F \times \frac{n_f^2(n_s + 1) - i n_f \tan(kd)(n_s + n_f^2)}{kd(n_s + n_f^2) - \tan(kd)(n_s + i kd(n_s + 1)n_f - n_f^2)}. \tag{10}$$

For an expression for σ_{xx} and σ_{xy} note that by the same symmetry assumed earlier the film dielectric permittivity tensor and the conductivity tensor are also diagonal in circular polarization, which we can convert to linear polarization as

$$\begin{aligned} \langle C | \sigma | C \rangle &= \begin{pmatrix} \sigma_p & 0 \\ 0 & \sigma_n \end{pmatrix}, \\ &= \langle C | L \rangle \langle L | \begin{pmatrix} \frac{\sigma_n + \sigma_p}{2} & \frac{i(\sigma_n - \sigma_p)}{2} \\ \frac{i(\sigma_p - \sigma_n)}{2} & \frac{\sigma_n + \sigma_p}{2} \end{pmatrix} | L \rangle \langle L | C \rangle. \end{aligned}$$

Using Maxwell’s equations the complex conductivity in CGS units is, therefore,

$$\sigma_{xx} = -\frac{i\omega}{8\pi} (n_{f,n}^2 + n_{f,p}^2) = -\frac{i\omega}{4\pi} n_f^2, \tag{11}$$

$$\sigma_{xx} = -\frac{i\omega}{8\pi} (n_{f,n}^2 + n_{f,p}^2) = \delta \frac{\omega}{4\pi} n_f. \tag{12}$$

By means of Eqs. (11) and (12), Eq. (10) becomes

$$\begin{aligned} \sigma_{xy} &= \theta_F \frac{\omega n_f^2}{2\pi} \\ &\times \frac{n_f(n_s + 1) - i \tan(kd)(n_s + n_f^2)}{kd(n_s + n_f^2) - \tan(kd)[n_s + i kd(1 + n_s)n_f - n_f^2]}. \end{aligned} \tag{13}$$

This expression, of course, requires accurate values for the real and imaginary parts of θ_F . Therefore the measurement system must be carefully characterized and calibrated, as is described in the next two sections.

C. Preliminary characterization and calibration

Calibrating the optical system is critical for two reasons. First, since the Faraday angle measurements are absolute, one must accurately calibrate the measurement system. Second, the calibration of the system reveals artifacts that may affect the validity of the measurements. In this section, we model our optical system and show that the system can be accurately calibrated. The S_2 and S_3 signals can be calibrated by placing a static wave plate with known retardance in front of the sample. The wave plate is mounted on a precision rotation stage. Using the analytical matrix techniques presented in Sec. III A, one can show that the S_2 and S_3 signals produced by a static wave plate are given by Eqs. (14a) and (14b):

$$S_2 = \frac{J_2(\beta)(1 - \cos R)\sin(4\phi)}{1 + \frac{1}{2}J_0(\beta)(1 - \cos R)\sin(4\phi)} \times D_2(\tau), \quad (14a)$$

$$S_3 = \frac{2J_3(\beta)\sin R \sin(2\phi)}{1 + \frac{1}{2}J_0(\beta)(1 - \cos R)\sin(4\phi)} \times D_3(\tau), \quad (14b)$$

where R is the wave-plate retardance, ϕ is the wave-plate orientation angle with respect to the incident laser polarization, D_n are the detector roll-off attenuation coefficients for the n th harmonic signal, and J_n are the n th order Bessel functions. Since the MCT detector that is used in these measurements has a response time on the order of $5 \mu\text{s}$, the detector roll-off must be included in the calibration. This roll-off will also produce phase shifts among the signals at harmonics of ω_m , which will distort the time-dependent detector signal and adversely affect any PEM calibration (as illustrated in Ref. 12) which relies on the shape of time-dependent wave form produced by the detector. The frequency dependence of the detector and its electronics was determined using a high-speed communications type laser diode to generate a known optical modulation at the same frequency and amplitude as that within the experimental system. When this beam was directed at the MCT detector the result corresponded well to the response of a simple RC circuit. Note that the wave-plate produces both polarization rotation (S_2) and polarization ellipticity (S_3) signals. These expressions are similar to Eqs. (5) and (6), with the wave plate mimicking the signal produced by $\text{Re}(\theta_F)$ and $\text{Im}(\theta_F)$ from a sample in a magnetic field.

Figure 4 shows typical calibration data using a static wave plate. Figures 4(a) and 4(b) show the S_2 and S_3 signals, respectively, as the wave plate is rotated over 360° (large-angle wave-plate calibration). Note the asymmetry of the peak heights in the S_2 signal in (a). This asymmetry is due to finite ellipticity in the incident laser beam. Calculations have determined that an ellipticity in the incident beam as small as 1 part in 10 000 when combined with an imperfect linear polarizer placed at 45° before the detector can lead to an anisotropy in the S_2 peaks of 6%. The measured leakage of

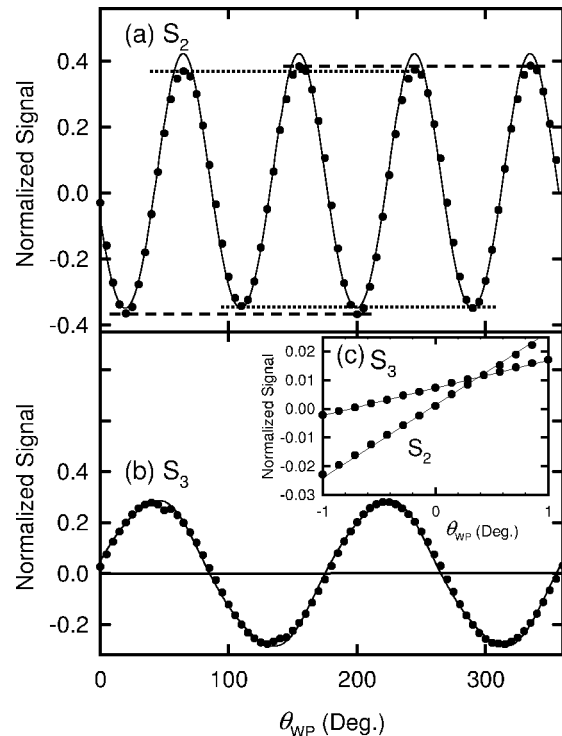


FIG. 4. Measurement (solid circles) of the S_2 (a) and S_3 (b) signals as a static wave plate is rotated 360° . The solid lines represents the predicted signals using independently measured parameters, e.g., wave-plate retardance, PEM retardance. The inset (c) shows these signals as a function of the wave-plate orientation angle between -1° and $+1^\circ$.

this polarizer is approximately 0.5%. The data (solid symbols) are compared to predictions (solid lines) that are based on earlier calibrations, including wave-plate retardance and PEM modulation amplitude.¹² The model fit (solid lines in Fig. 4) uses the detector roll-off frequency as the sole fitting parameter, and this frequency is in good agreement with the roll-off frequency result obtained independently using the high-speed communications type laser diode measurement. In practice, this calibration technique is only concerned with the values of the normalized signals at extrema, e.g., 22.5° , 45° , and 67.5° .

Since the large-angle wave-plate calibration technique depends on the extremal values of the signal as the wave-plate is rotated, accurate measurement of the wave-plate orientation is not critical. However, the anisotropy of the signal for even harmonics makes precise calibration difficult. Furthermore, we are interested in measuring very small Faraday signals where the laser polarization is only slightly affected by the sample, while the large-angle techniques create large changes in the laser polarization. Therefore, a second technique was developed to measure small Faraday signals. This technique (referred to as the small-angle calibration) is identical to the large-angle wave-plate calibration except that the range of wave-plate orientation angle ϕ is only several degrees about a null signal (where $\phi=0$). The results of the small-angle wave-plate calibration measurements are shown in Fig. 4(c). Note the linear behavior of S_2 and S_3 for this small-angle range. Since the detector/electronics roll-off frequency was determined by the large-angle-waveplate calibration, no fitting parameters are used for the small-angle-

wave-plate calibration model [solid lines in Fig. 4(c)]. Since the Faraday signals are normalized by the average transmission, drift in laser power or detector gain is almost exactly canceled out. In fact, the stability of the signals at a fixed wave-plate orientation is better than 1 part in 10 000 over a 10 min period. In fact, as long as the laser polarization is stable, the laser power can change by an order of magnitude without changing the Faraday signals perceptibly. Calibration measurements for the first four harmonics of ω_m (S_1 and S_4 as well as S_2 and S_3) of ω_m were performed over the entire experimental wavelength range and produced similar agreement with the model. The S_2 signal also can be calibrated by replacing the waveplate with a linear polarizer, which causes an accurately known absolute Faraday rotation.

D. Routine calibration

Though the success in modeling the extensive calibration measurements is reassuring, once the the measurement system is well characterized, the calibration for individual runs can be greatly simplified. Typically, the Faraday rotation is calibrated immediately before a run with the sample in place by rotating the PEM by a known small angle using a sine bar. A simple method arises for obtaining $\text{Re}(\theta_F)$, which makes use of the provision for physically rotating the PEM assembly back and forth a predetermined amount as discussed previously. For small rotations, this is equivalent to rotating a linear polarizer at the sample position, as mentioned in the previous section. Prior to collecting each data set for each laser line one rotates the PEM assembly back and forth by the predetermined amount and records the readings from the lock-in amplifiers. For small-angle rotations ϕ , where $\sin \phi \rightarrow \phi \rightarrow 0$, the relationship between S_2 and ϕ is

$$S_2 = 4\phi J_2(\beta) D_2(\tau). \quad (15)$$

The real rotation of the PEM from a known initial angle of ϕ^a to a known final angle ϕ^b , and the fact that S_2 is linear with ϕ , are used to define the calibration factor C_{real} for $\text{Re}(\theta_F)$ as follows:

$$C_{\text{real}} = \frac{\phi^b - \phi^a}{S_2^b - S_2^a}, \quad (16)$$

where S_2^a and S_2^b are the initial and final readings corresponding to ϕ^a and ϕ^b , respectively.

This calibration procedure also supplies the sign of $\text{Re}(\theta_F)$, which the electronics by itself leaves ambiguous. Since this calibration procedure relates observed changes in S_2 to known changes in the polarization, a separate calibration of the optical and electrical components is not required, and therefore, any errors that these elements may introduce can be avoided. Subsequent to this calibration, $\text{Re}(\theta_F)$ emerges from the data as

$$\text{Re}(\theta_F) = (\text{sign}) \times S_2^{\text{data}} \times C_{\text{real}}, \quad (17)$$

where S_2^{data} is the signal corresponding to the Faraday rotation induced by a sample.

Because the frequency dependence of $\text{Im}(\theta_F)$, typically, is also weak, its determination also requires data with very high relative accuracy. Equation (5), along with the rotation

calibration above, also afford a relative calibration for $\text{Im}(\theta_F)$. This calibration is essential in order to reliably determine the correspondingly small wavelength dependence of $\text{Im}(\theta_F)$. The procedure entails simply comparing the actual, predetermined, physical rotation with the calculated value from Eq. (5) and then adjusting the value of the PEM retardance β in Eq. (5), until they agree. When calculating $\text{Im}(\theta_F)$ with Eq. (6) we use this adjusted value β_{adj} in place of that determined from the manufacturers calibration. This procedure should be performed initially, and then after each laser line change. Here, again, the electronics leave the sign ambiguous, so it must be determined using a sample of known ellipticity such as a quarter-wave plate. Combining the foregoing calibration corrections:

$$\text{Im}(\theta_F) = (\text{sign}) \frac{1}{\pi J_3(\beta_{\text{adj}})} S_3(\lambda). \quad (18)$$

The final element in calibrating the polarization signal involves removing background contributions to S_2 arising from the sample substrate and ZnSe magnet windows. The background contribution to θ_F manifests itself as a number of terms:

$$\theta_{F,\text{background}} = c_0 + c_1 B + c_2 B^2 + \dots, \quad (19)$$

where each coefficient c_i may have a wavelength dependence. In the current work the data sets contain θ_F as a function of magnetic field which is, for example, scanned from +8 to -8 T or vice versa. From these data we compute the slope $\partial\theta_F/\partial B$, which obviously does not contain c_0 . Further, because the magnetic field values are both positive and negative, computation of the average slope eliminates all terms even in \mathbf{B} . Removing the remaining odd terms requires direct measurement of the background using a sample of the substrate material followed by simple subtraction of the result from the data sets. Fortunately, since the windows and substrates are isotropic and do not absorb the MIR radiation, no background ellipticity is introduced into the beam via linear birefringence or circular dichroism, respectively. As a result, no background subtraction is required for the S_3 [$\text{Im}(\theta_F)$]. The results of these measurements for substrates of BaF and high purity Si were purely real Faraday angles, which were consistent with the band gaps of these substrate materials and the ZnSe magnet housing windows as well as the absence of free carriers.

IV. EXPERIMENTAL MEASUREMENTS

A. Semiconductors

Faraday measurements were first performed on semiconductor samples for three reasons. First, the signals are large and can be readily increased by using thicker samples. Second, the optical properties of semiconductors are well known, which allows the accuracy of the Faraday measurements to be verified by comparing them to the results reported in other experiments. Finally, since the thin-film samples are grown on semiconductors, it is important to measure their contribution to the Faraday signals accurately in order to remove these backgrounds from the desired thin-film signals.

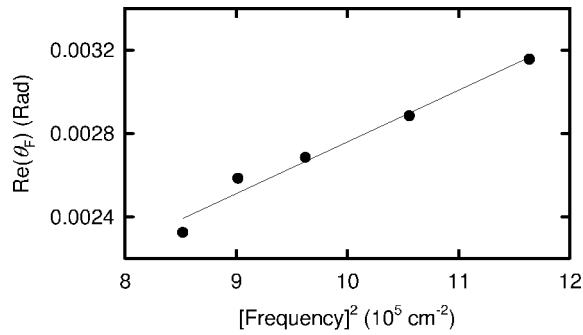


FIG. 5. $\text{Re}(\theta_F)$ as a function of frequency squared at 8 T for a GaAs sample. The solid line represents a ω^2 fit. The semi-insulating sample is wedged with an average thickness of 0.42 mm.

The Faraday measurements were performed on three semiconductors. In semiconductors, two sources contribute to the θ_F .¹³ The first source is from free carriers, which have a contribution to the θ_F that is proportional to ω^{-2} , where ω is the radiation frequency. The second source is from interband transitions, where the magnetic field causes anisotropy in the absorption and refractive index for left and right circularly polarized light. For the MIR radiation used in this experiment, where the photon energies are approximately an order of magnitude smaller than the energy band gap in typical semiconductors, no absorption occurs and the interband contribution is restricted to an anisotropy in the index of refraction for left and right circularly polarized modes. This difference in index leads to a phase shift between left and right circularly polarized light, which in turn results in a rotation of the incident linear polarization (Faraday rotation). For radiation below the band gap, the interband contribution to Faraday rotation is proportional to ω^2 . Furthermore, since the semiconductors in this experiment are of high purity and the MIR frequencies are relatively high, the free-carrier contribution is minimized. Faraday rotation caused by such samples is quantified in terms of its Verdet constant V , which is defined as the angle of rotation per unit magnetic field per unit thickness of the sample. The frequency dependence of the Verdet constant and its relationship to the Faraday angle at 8 T for a semiconductor is given by the following equation:¹⁴

$$V = u\omega^2 + \frac{v}{\omega^2} = \frac{\text{Re}[\theta_F(8\text{T})]}{8\text{T} \times D} \times \frac{180}{\pi}, \quad (20)$$

where u is the coefficient for the interband contribution and v is the coefficient for the free-carrier contribution to the Faraday rotation, and D is the sample thickness. In Ref. 14, the Verdet constant as a function of frequency was measured (2000–3300 cm^{-1} for several Si samples with different free-carrier concentrations). One can extend these results to 949 cm^{-1} by using Eq. (20) to obtain u and v from the data in Ref. 14. The Verdet coefficient at 949 cm^{-1} is estimated to be 25.0°/T m. The value obtained at that frequency and 293 K by our MIR Faraday measurements on a high purity (>1 k Ω cm) silicon sample is 25.6°/T m. This corresponds to $\text{Re}[\theta_F] = 2 \times 10^{-3}$ at 8 T and 949 cm^{-1} for a 0.50-mm-thick sample.

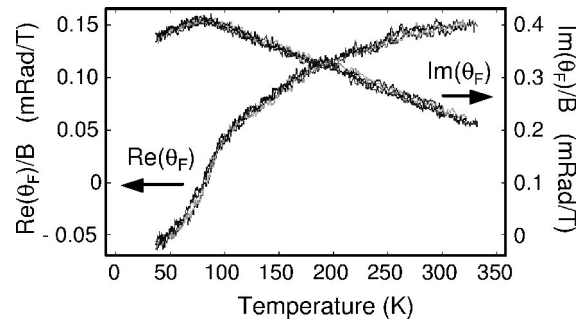


FIG. 6. $\text{Re}(\theta_F)$ and $\text{Im}(\theta_F)$ each per Tesla and vs temperature for 2212 BSCCO measured at 950 cm^{-1} . Each trace represents a different subtracted pair of temperature scans. There are four pairs total in each graph.

The second semiconductor material is semi-insulating GaAs. In this case, the frequency dependence of the Faraday rotation signal is explored. Figure 5 plots $\text{Re}(\theta_F)$ as a function of frequency squared at 8 T and 293 K for a GaAs sample. The solid line represents a ω^2 fit. The semi-insulating sample is wedged with an average thickness of 0.42 mm. The ω^2 frequency behavior of $\text{Re}(\theta_F)$ is consistent with Eq. (20). At 8 T and 949 cm^{-1} , $\text{Re}(\theta_F)$ is approximately 3×10^{-3} . The Verdet coefficient is approximately 44°/T m. The value obtained at 10.59 μm for Cr-doped¹⁵ GaAs by Ref. 16 is 41°/T m. This is approximately 50% larger than that for Si, which is consistent with the fact that GaAs has a direct band gap that is approximately a factor of 2 smaller than that of Si. This brings the MIR radiation in GaAs closer to the refractive index anisotropy at the band edge. In fact, the $\text{Re}(\theta_F)$ for GaAs decreased as the temperature is lowered, which is consistent with the increase in the band gap as the temperature decreases. As expected, no circular dichroism signal is observed ($\text{Im}[\theta_F] \approx 0$).

The final semiconductor investigated is LaSrGaO₄. This material has the largest band gap, and hence, the smallest interband contribution to $\text{Re}(\theta_F)$. At 8 T, 293 K, and 949 cm^{-1} , the $\text{Re}(\theta_F)$ is approximately 5.2×10^{-4} rad for a 0.31-mm-thick sample. This translates in a Verdet coefficient at 949 cm^{-1} of 12°/T m. To the authors' best knowledge, this is the first reported measurement of the MIR Verdet coefficient in LaSrGaO₄. Despite the onset of strong absorption by phonons for radiation below 1000 cm^{-1} , LaSrGaO₄ proved to be an excellent substrate due to its weak contribution to the $\text{Re}(\theta_F)$ background. Note that as the frequency is decreased, the strength of the semiconductor Faraday signals decreases [Eq. (20)] while the signal from the free carriers in the thin-film metallic samples increases [Eq. (20)]. As a result, the lower frequency measurements are simpler and more accurate.

B. High temperature superconductor $\text{Bi}_2\text{Sr}_2\text{Ca}_1\text{Cu}_2\text{O}_{8+\delta}$

The measurements also include the response of $\text{Bi}_2\text{Sr}_2\text{Ca}_1\text{Cu}_2\text{O}_{8+\delta}$ to input radiation from 920 to 1090 cm^{-1} and over a temperature range from 30 to 330 K in an external B field ranging from -8 to $+8$ T. Figure 6 depicts θ_F versus temperature. The Hall angle $\theta_H = \sigma_{xy}/\sigma_{xx}$ in this case exhibits similar behavior and can be

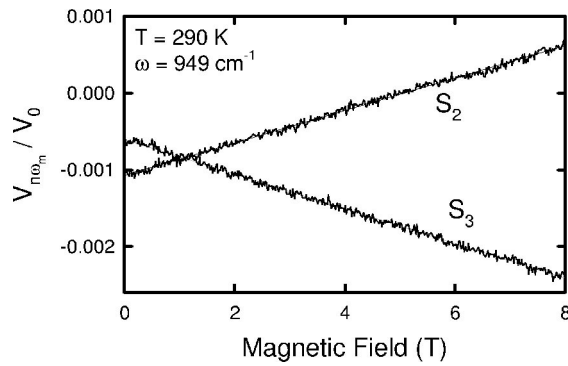


FIG. 7. S_2 and S_3 normalized signals for a Cu film as a function of magnetic field at 949 cm^{-1} and 290 K .

readily obtained from θ_F .^{7,8} In fact, the values obtained for θ_H in this particular run are within 10% of θ_F . To form θ_H one would usually divide σ_{xy} by the value of σ_{xx} corresponding to the same temperature and frequency. But, here, we wish to examine that part of the Hall angle related to the free carriers. Interband transitions which are on the order of 1 V contribute essentially nothing to σ_{xy} . However, we must remove their somewhat more substantial contribution to σ_{xx} before taking the ratio. In CGS units

$$\epsilon_{\text{total}} = \epsilon_{\text{bound}} + i \frac{4\pi\sigma_{\text{free}}}{\omega} = i \frac{4\pi\sigma_{\text{total}}}{\omega}, \quad (21)$$

$$\sigma_{\text{free}} = \sigma_{\text{total}} + \frac{i\omega\epsilon_{\text{bound}}}{4\pi}. \quad (22)$$

As with θ_F in Fig. 6, $\text{Re}(\theta_H)$ increases with temperature but appears to saturate around 300 K. $\text{Re}(\theta_H)$ is positive for all temperatures in the normal state and does not show any striking discontinuity at T_c at 90 K. These data appear in Ref. 9 where it is compared with far-infrared data from Ref. 17. The results show a significant disconnect from the behavior of $\text{Re}(\theta_H)$ in the existing data for $\text{YBa}_2\text{Cu}_3\text{O}_7$ in the far infrared, which indicate a negative value for $\text{Re}(\theta_F)$ above 250 cm^{-1} , whereas that of the current work at 1000 cm^{-1} is positive. The current work when analyzed using an extended Drude formalism results in a Hall mass comparable to the angular-resolved photoemission spectroscopy (ARPES) Fermi mass and a scattering rate comparable to the dc longitudinal, dc Hall, and far-infrared Hall scattering rates, which, however, are only $\frac{1}{4}$ of the ARPES values.

C. Metal films

Figure 7 shows the S_2 and S_3 signals as a function of magnetic field B at room temperature for a Cu thin-film sample. The MIR radiation frequency is 949 cm^{-1} . The background contribution due to the substrate and windows has not been removed. Note the negative offset in the S_2 data. The signals are linear in B , as expected.

It is interesting to compare the MIR Hall effect results on HTSC (Refs. 8, 9, and 18) with those on Au and Cu films.^{2,7} Surprisingly, the Hall angle results for both materials are qualitatively similar, and are well parametrized by the Drude form for θ_H . For both systems, the scattering rate γ_H associated with the Hall angle is linear in temperature and

independent of frequency. In Au and Cu the longitudinal scattering rate γ_{xx} (obtained from infrared conductivity measurements) is also temperature dependent and frequency independent as expected from electron-phonon scattering when the measurement frequency is higher than the Debye frequency. For optimally doped $\text{YBa}_2\text{Cu}_3\text{O}_7$ in the MIR, however, while γ_H has a strong temperature dependence and no frequency dependence, γ_{xx} is temperature independent but frequency dependent [as found in infrared conductivity¹⁹ and ARPES (Ref. 20)]. The behavior of γ_{xx} precludes phonons or magnons as the dominant scatterers, and the lack of frequency dependence of γ_H is in contrast to the predicted and observed behavior of a Fermi liquid or inelastic scattering in general. Therefore, the frequency and temperature dependence of γ_H that are reported in the MIR (Ref. 8) are highly unusual and indicate a non-Fermi liquid behavior of the normal state of $\text{YBa}_2\text{Cu}_3\text{O}_7$. Similar results have been obtained recently in other HTSC materials such as optimally doped $\text{Bi}_2\text{Sr}_2\text{CaCu}_2\text{O}_8$ (Ref. 9) and underdoped $\text{YBa}_2\text{Cu}_3\text{O}_7$.¹⁸ These results are not yet understood. Ioffe and Millis²¹ have recently proposed a model of quasi-elastic scattering from superconducting fluctuations in the normal state of high T_c materials that leads to a relaxation rate behavior similar to that observed. Effects attributed to superconducting fluctuations have also been observed in the normal state of underdoped $\text{Bi}_2\text{Sr}_2\text{CaCu}_2\text{O}_8$ in measurements of the longitudinal conductivity by THz spectroscopy.²² While no interpretation of these experiments is widely accepted it is clear that the frequency and temperature dependence of the Hall response of the normal state in HTSC serves as a critical test for any theoretical interpretation of the exotic properties of these materials.

ACKNOWLEDGMENTS

The authors wish to extend their thanks to G. S. Jenkins, J. R. Simpson, and D. B. Romero for their assistance in performing the various reported measurements, and G. Gu and J. J. Tu for supplying the BSCCO sample and transport data. This work was supported by the NSF under Contract No. DMR 0070959

APPENDIX A: POLARIZATION ANALYSIS USING DIRAC NOTATION

In polarimetric measurements a train of optical components, along with a sample, modify or operate on an input beam, which is in some state of known intensity and polarization. Optical components typically include somewhat imperfect devices such as polarizers, wave plates, photoelastic modulators, and mechanical rotators. The modified output beam generally strikes a detector producing an output electrical signal. Here, we develop a general formalism useful in relating the electrical signal to the properties of the sample. The formalism uses Dirac notation, which well differentiates between a vector or state $|\psi\rangle$ and its representation in some basis: $\langle x|\psi\rangle$. In polarimetry the usual bases are linear and circular polarizations. The formalism also replaces the Jones matrices with generalized operators and introduces the basis transformations and geometrical rotation operations. Finally, the result is related to the output of the typical square-law optical detector.

In what follows, the direction of propagation is in the positive z direction and all angles are measured in the positive radial direction off the x axis and about the z axis. Beginning with the input beam, the formalism simply considers it to be a non-normalized ket

$$|\text{in}\rangle.$$

Expressed in the linear polarization basis it is

$$|\text{in}\rangle = \sum_L |L\rangle \langle L|\text{in}\rangle = |x\rangle \langle x|\text{in}\rangle + |y\rangle \langle y|\text{in}\rangle,$$

or in the circular basis

$$|\text{in}\rangle = \sum_C |C\rangle \langle C|\text{in}\rangle = |p\rangle \langle p|\text{in}\rangle + |n\rangle \langle n|\text{in}\rangle,$$

where $|p\rangle$ indicates an electric vector rotating in the positive radial direction about the z axis as seen at a fixed point and $|n\rangle$ indicates an electric vector rotating in the negative radial direction about the z axis also as seen at a fixed point. $|p\rangle$ and $|n\rangle$ are also referred to as having positive and negative helicity. In matrix notation

$$\langle L|\text{in}\rangle = \begin{pmatrix} E_x \\ E_y \end{pmatrix} \quad \text{and} \quad \langle C|\text{in}\rangle = \begin{pmatrix} E_p \\ E_n \end{pmatrix}.$$

The various components in the optical train appear as operators acting on the input ket to produce the output ket:

$$|\text{out}\rangle = \mathbf{TVW}|\text{in}\rangle.$$

In the linear basis this is

$$\begin{aligned} |\text{out}\rangle &= |L\rangle \langle L|TVW|L'\rangle |\text{in}\rangle \\ &= |L\rangle \langle L|T|L''\rangle \langle L''|V|L''' \rangle \langle L'''|W|L'\rangle \langle L'\rangle |\text{in}\rangle \\ &= |L\rangle \langle L|T|L\rangle \langle L|V|L\rangle \langle L|W|L\rangle \langle L|\text{in}\rangle, \end{aligned}$$

where summation is assumed over repeated state designations L ; and the primes have been dropped with the understanding that the order of the matrices will not be changed.

Some devices or operations such as geometric and Faraday rotations are most easily represented in the circular basis. The transformation matrices, $\langle C|L\rangle$ and $\langle L|C\rangle$, are the means of conversion between these two bases. The transformation for states proceeds as

$$\begin{aligned} |\text{in}\rangle &= \sum_L |L\rangle \langle L|\text{in}\rangle \\ &= \sum_{LC} |C\rangle \langle C|L\rangle \langle L|\text{in}\rangle \\ &= |C\rangle \langle C|L\rangle \langle L|\text{in}\rangle, \end{aligned}$$

and for operators as

$$\begin{aligned} \mathbf{T} &= \sum_{L,L'} |L\rangle \langle L|\mathbf{T}|L'\rangle \langle L'| \\ &= \sum_{L,L'} \sum_{C,C'} |C\rangle \langle C|L\rangle \langle L|\mathbf{T}|L'\rangle \langle L'|C\rangle \langle C| \\ &= |C\rangle \langle C|L\rangle \langle L|\mathbf{T}|L\rangle \langle L|C\rangle \langle C|. \end{aligned}$$

In matrix representation

$$\langle C|L\rangle = \frac{1}{\sqrt{2}} \begin{pmatrix} 1 & -i \\ 1 & i \end{pmatrix} \quad \text{and} \quad \langle L|C\rangle = \frac{1}{\sqrt{2}} \begin{pmatrix} 1 & 1 \\ i & -i \end{pmatrix}.$$

Below are the representations of some simple optical components in the linear bases: a perfect polarizer aligned along the x axis

$$\begin{pmatrix} 1 & 0 \\ 0 & 0 \end{pmatrix},$$

a $\frac{1}{4}$ wave plate aligned with slow axis along the x axis

$$\begin{pmatrix} e^{i(\pi/2)} & 0 \\ 0 & 1 \end{pmatrix},$$

and a photoelastic modulator aligned along the x axis

$$\begin{pmatrix} e^{i\beta \cos(2\pi ft)} & 0 \\ 0 & 1 \end{pmatrix}.$$

Another concern for the devices or components is their orientation. Assume, for example, that the operator T represents the effect of some component such a polarizer which is aligned with its critical direction at an angle θ from the x axis. A simple rotation operation develops an expression for the rotated polarizer:

$$T(\theta) = \mathbf{RTR}^{-1},$$

where R is an active rotation and in circular representation is

$$\langle C|\mathbf{R}(\theta)|C\rangle = \begin{pmatrix} e^{-i\theta} & 0 \\ 0 & e^{i\theta} \end{pmatrix}.$$

Finally, the output of a square-law type optical detector, aside from any responsivity factor, is for our example

$$d(t) \propto \langle \text{out}|\text{out}\rangle,$$

where $|\text{out}\rangle$ is the Hermitian conjugate of $\langle \text{out}|$.

APPENDIX B: MULTILAYER RESPONSE USING RELATIVE IMPEDANCE MATRICES

Assume that some layered materials are arranged normal to the z axis and we desire a formalism for the transmitted and reflected intensities for plane waves incident at arbitrary angles. To begin, the plane wave solution to Maxwell's equations is

$$\mathbf{E}_{i,\pm} = \mathcal{E}_{i,\pm} e^{i\mathbf{k}_{i,\pm} \cdot \mathbf{r} - i\omega t}, \quad (\text{B1})$$

$$\mathbf{H}_{i,\pm} = \mathcal{H}_{i,\pm} e^{i\mathbf{k}_{i,\pm} \cdot \mathbf{r} - i\omega t}, \quad (\text{B2})$$

where $+$ represents a wave traveling in the positive z direction at some otherwise arbitrary angle, $-$ represents a wave traveling in the negative z direction, and i is the layer number. Then, in CGS:

$$\begin{aligned} \mathbf{H}_{i,\pm} &= \sqrt{\frac{\epsilon_i}{\mu_i}} \hat{\mathbf{k}}_{i,\pm} \times \mathbf{E}_{i,\pm}, \\ &= \frac{1}{Z_i} \hat{\mathbf{k}}_{i,\pm} \times \mathbf{E}_{i,\pm}, \quad \text{CGS}, \end{aligned} \quad (\text{B3})$$

where $\hat{k}_{i,\pm}$ is a unit vector parallel to the propagation direction, ϵ_i is the complex dielectric constant of the i th layer and includes all conductivity effects, and $Z_i = \sqrt{\mu_i/\epsilon_i}$ is the relative impedance of the medium, and like ϵ may be complex.

Now that we have a solution inside a layer we need to match solutions for different layers at the boundaries between layers. The curl E Maxwell equation provides one boundary condition:

$$\mathbf{E}_i \times \hat{z} = \mathbf{E}_{i+1} \times \hat{z}. \quad (\text{B4})$$

The curl H Maxwell equation provides the other boundary condition:

$$\mathbf{H}_i \times \hat{z} = \mathbf{H}_{i+1} \times \hat{z}. \quad (\text{B5})$$

To apply the foregoing consider first S polarization (E perpendicular to the plane of incidence) at each side of a boundary. In such an instance the E field is tangent to the boundary and if we orient the x and y axes so that E is also perpendicular to the y axis, then, from Eq. (B4):

$$\mathcal{E}_{i,+x} + \mathcal{E}_{i,-x} = \mathcal{E}_{i+1,+x} + \mathcal{E}_{i+1,-x}. \quad (\text{B6})$$

Likewise, substituting Eq. (B3) into Eq. (B5) produces:

$$\begin{aligned} \frac{\cos(\theta_i)}{Z_i} (\mathcal{E}_{i,+x} - \mathcal{E}_{i,-x}) \\ = \frac{\cos(\theta_{i+1})}{Z_{i+1}} (\mathcal{E}_{i+1,+x} - \mathcal{E}_{i+1,-x}), \end{aligned} \quad (\text{B7})$$

where θ_i is the angle of incidence measured of the z axis. Defining the incident impedance for S polarization as

$$Z_{S,i} = \frac{Z_i}{\cos(\theta_i)}, \quad (\text{B8})$$

Eq. (B7) becomes

$$\frac{1}{Z_{S,i}} (\mathcal{E}_{i,+x} - \mathcal{E}_{i,-x}) = \frac{1}{Z_{S,i+1}} (\mathcal{E}_{i+1,+x} - \mathcal{E}_{i+1,-x}). \quad (\text{B9})$$

Combining Eqs. (B6) and (B9) into a matrix form:

$$\begin{pmatrix} \mathcal{E}_{i+1,+} \\ \mathcal{E}_{i+1,-} \end{pmatrix} = \mathbf{S}_{i,i+1} \begin{pmatrix} \mathcal{E}_{i,+} \\ \mathcal{E}_{i,-} \end{pmatrix}, \quad (\text{B10})$$

where

$$\mathbf{S}_{i,i+1} = \frac{1}{2Z_{S,i}} \begin{pmatrix} Z_{S,i} + Z_{S,i+1} & Z_{S,i} - Z_{S,i+1} \\ Z_{S,i} - Z_{S,i+1} & Z_{S,i} + Z_{S,i+1} \end{pmatrix}. \quad (\text{B11})$$

For \mathbf{P} polarization (\mathbf{E} field \parallel to plane of incidence) define the incident admittance as

$$Y_{P,i} = \frac{1}{\cos(\theta_i)Z_i}, \quad (\text{B12})$$

then following the same procedure:

$$\begin{pmatrix} \mathcal{H}_{i+1,+} \\ \mathcal{H}_{i+1,-} \end{pmatrix} = \mathbf{P}_{i,i+1} \begin{pmatrix} \mathcal{H}_{i,+} \\ \mathcal{H}_{i,-} \end{pmatrix}, \quad (\text{B13})$$

where

$$\mathbf{P}_{i,i+1} = \frac{1}{2Y_{P,i}} \begin{pmatrix} Y_{P,i} + Y_{P,i+1} & Y_{P,i} - Y_{P,i+1} \\ Y_{P,i} - Y_{P,i+1} & Y_{P,i} + Y_{P,i+1} \end{pmatrix}. \quad (\text{B14})$$

The E field can be determined from H using Eq. (B3).

Equations (B8), (B10), and (B11) and Eqs. (B12), (B13), and (B14) provide the incident and reflected amplitudes in the $i+1$ layer at the interface in terms of the amplitudes in the i layer at the interface for \mathbf{S} and \mathbf{P} polarization, respectively. It remains to develop the equations to propagate the amplitudes across layer i of thickness d_i . This is already provided by Eqs. (B1) and (B2), which in matrix form become

$$\begin{aligned} \begin{pmatrix} \mathcal{E}_{i,+}(z=d_i) \\ \mathcal{E}_{i,-}(z=d_i) \end{pmatrix} &= \begin{pmatrix} e^{-ik_{i,+}\hat{z}d_i} & 0 \\ 0 & e^{ik_{i,-}\hat{z}d_i} \end{pmatrix} \begin{pmatrix} \mathcal{E}_{i,+}(z=0) \\ \mathcal{E}_{i,-}(z=0) \end{pmatrix} \\ &= \mathbf{U}_i \begin{pmatrix} \mathcal{E}_{i,+}(z=0) \\ \mathcal{E}_{i,-}(z=0) \end{pmatrix}. \end{aligned}$$

So, as an example, given a set of layers numbered 1 to n from left to right, the equation relating the incident and reflected amplitudes on the left side of the set to the right side for \mathbf{S} polarization is

$$\begin{aligned} \mathbf{S}_{n-1,n} \mathbf{U}_{n-1} \mathbf{S}_{n-2,n-1} \cdots \mathbf{U}_{i+1} \mathbf{S}_{i,i+1} \begin{pmatrix} \mathcal{E}_{i,+}(\text{left}) \\ \mathcal{E}_{i,-}(\text{left}) \end{pmatrix} \\ = \begin{pmatrix} \mathcal{E}_{n,+}(\text{right}) \\ \mathcal{E}_{n,-}(\text{right}) \end{pmatrix}. \end{aligned}$$

- ¹J. M. Harris, Y. F. Yan, and N. P. Ong, Phys. Rev. B **46**, 14293 (1992).
- ²H. D. Drew, S. Wu, and H.-T. S. Lihn, J. Phys.: Condens. Matter **8**, 10037 (1996).
- ³H. D. Drew and P. Coleman, Phys. Rev. Lett. **78**, 1572 (1997).
- ⁴L. D. Landau, Sov. Phys. JETP **3**, 920 (1957); **5**, 101 (1957); **8**, 70 (1959).
- ⁵See, for example, S. G. Kaplan, S. Wu, H.-T. S. Lihn, H. D. Drew, Q. Li, D. B. Fenner, J. M. Phillips, and S. Y. Hou, Phys. Rev. Lett. **76**, 696 (1996).
- ⁶Y. Tokura, A. Urushibara, Y. Moritomo, T. Arima, A. Asamitsu, G. Kido, and N. Furukawa, J. Phys. Soc. Jpn. **63**, 3931 (1994); K. Chahara, T. Ohno, M. Kasai, and Y. Kozono, Appl. Phys. Lett. **63**, 1990 (1993); R. v. Helmholtz, J. Wecker, B. Holzapfel, L. Schultz, and K. Samwer, Phys. Rev. Lett. **71**, 2331 (1993); S. Jin, T. H. Tiefel, M. McCormack, R. A. Fastnacht, R. Ramesh, and L. H. Chen, Science **264**, 413 (1994); S. G. Kaplan, M. Quijada, H. D. Drew, D. B. Tanner, G. C. Xiong, R. Ramesh, C. Kwan, and T. Venkatesan, Phys. Rev. Lett. **77**, 2081 (1996).
- ⁷J. Černe, D. C. Schmadel, M. Grayson, G. S. Jenkins, J. R. Simpson, and H. D. Drew, Phys. Rev. B **61**, 8133 (2000).
- ⁸J. Černe, M. Grayson, D. C. Schmadel, G. S. Jenkins, H. D. Drew, R. Hughes, J. S. Preston, and P. J. Kung, Phys. Rev. Lett. **84**, 3418 (2000).
- ⁹D. C. Schmadel, J. J. Tu, L. B. Rigal, D. B. Romero, M. Grayson, and H. D. Drew, arXiv:cond-mat/0210304 (2002).
- ¹⁰R. Burdett, Perkin Elmer Instruments, 4/12/00 Application Note No. 1003.
- ¹¹R. Burdett, Perkin Elmer Instruments, 4/12/00 Application Note No. 1001.
- ¹²Several techniques for calibrating the PEM retardance amplitude are described in Appendix A, PEM-90 Photoelastic Modulator Systems User Manual from Hinds Instruments (1998).
- ¹³I. G. Mavroides, in *Optical Properties of Solids*, edited by F. Abelès (North-Holland, Amsterdam, 1972).
- ¹⁴G. Ruymbeek, W. Greendonk, and P. Nagels, Physica B & C **89**, 14 (1977).

- ¹⁵Since the free-carrier contribution to V falls off with frequency as ω^{-2} , we do not expect this doping to strongly affect V at 1000 cm^{-1} . Therefore, measurements of V on doped and undoped GaAs should be comparable at 1000 cm^{-1} .
- ¹⁶C. R. Phipps, S. J. Thomas, and B. Lax, *Appl. Phys. Lett.* **25**, 313 (1974).
- ¹⁷M. Grayson, L. B. Rigal, D. C. Schmadel, H. D. Drew, and P. J. Kung, *Phys. Rev. Lett.* **89**, 037003 (2002).
- ¹⁸L. B. Rigal, D. C. Schmadel, H. D. Drew, B. Maiorov, E. Osquigil, J. S. Preston, R. Hughes, and G. D. Gu, *cond-mat/0309108* (2003).
- ¹⁹Z. Schlesinger, R. T. Collins, F. Holtzberg, C. Feild, G. Koren, and . Gupta, *Phys. Rev. B* **41**, 11237 (1990).
- ²⁰T. Valla, A. V. Fedorov, P. D. Johnson, B. O. Wells, S. L. Hulbert, Q. Li, G. D. Gu, and N. Koshizuka, *Science* **285**, 2110 (1999); A. Kaminski, J. Mesot, H. Fretwell, J. C. Campuzano, M. R. Norman, M. Randiera, H. Ding, T. Sato, T. Takahashi, T. Mochiku, K. Kadowaki, and H. Hoehst, *Phys. Rev. Lett.* **84**, 1788 (2000).
- ²¹L. B. Ioffe and A. J. Millis, *Phys. Rev. B* **58**, 11631 (1998).
- ²²J. Corson, R. Mallozzi, J. Orenstein, J. N. Eckstein, and I. Bozovic, *Nature (London)* **398**, 22 (1999).